Robotica (2026), **44**, pp. 1305–1324
doi:10.1017/S0263574726103580

CAMBRIDGE UNIVERSITY PRESS

RESEARCH ARTICLE

Mechanism design and trajectory planning of a kinematically redundant parallel climbing robot

Wei Ye, Tongwang Huo and Xintian Feng

School of Mechanical Engineering, Zhejiang Sci-Tech University, Hangzhou, China
Corresponding author: Wei Ye; Email: wye@zstu.edu.cn

Received: 18 February 2025 UTC; **Revised:** 25 April 2026 UTC; **Accepted:** 14 May 2026 UTC;
First published online: 23 June 2026 UTC

Keywords: kinematically redundant parallel mechanism; climbing robot; global path planning; local path planning; single-step motion planning

Abstract

This paper proposes a kinematically redundant wall-climbing robot (CR), which employs a kinematically redundant parallel mechanism (PM) as its main body, combined with a serial mechanism, to achieve wall-climbing motion and avoid the dangers associated with manual operation. The improved Grübler-Kutzbach formula is utilized to analyze the degrees of freedom (DOF) of the PM. Subsequently, a kinematic analysis covering position, velocity, singularity, and workspace is conducted to establish the theoretical basis for the robot's motion planning. To cope with complex working environments, trajectory planning is carried out for the CR, and the complex path planning problem in space is addressed through hierarchical processing, including global path planning, local path planning, and single-step motion planning. After theoretical analysis, kinematic, singularity, workspace analysis, and trajectory planning method of the proposed CR were verified through simulation experiments, confirming the correctness of the kinematic modeling and trajectory solution. Finally, a physical prototype was built to verify the climbing capability of the robot.

1. Introduction

With the development and construction of cities, high-altitude operations such as cleaning glass curtain walls and inspecting transmission towers are becoming increasingly common. Traditional manual methods are not only inefficient but also pose significant safety risks. Therefore, replacing manual operations with machines has become a hot research topic in recent years [1–5]. Scholars both domestically and internationally have conducted extensive research on climbing robots (CRs), developing a series of wall-CRs that can perform tasks such as inspection and maintenance.

CRs can be roughly categorized into four types based on their structure. The first type is wheeled/tracked robots. For example, Hu et al. [6] developed a permanent magnetic tracked CR that uses tracks as both its walking and adhesion mechanisms, offering strong adhesion and high load-bearing capacity. Cai et al. [7] proposed a CR that uses wheels for movement and adhesion, which features high speed. The second type is serial robots. Inspired by crawling animals like inchworms, Guan et al. [8–10] developed a modular CR capable of three different climbing gaits. This CR has a large workspace and strong obstacle-crossing ability. The third type is parallel robots. Saltaren et al. [11, 12] proposed a six degrees of freedom (DOFs) CR, characterized by its strong load-bearing capacity and high accuracy. The fourth type is hybrid robots. Yao et al. [13] designed a transmission tower inspection CR with two identical parallel mechanisms (PMs) as its legs, connected by a central link mechanism, enabling it to climb and overcome obstacles. Son et al. [14] designed a wheel-leg hybrid CR capable of adapting to complex environments.

In practical applications, the aforementioned CRs have certain limitations and cannot fully meet the requirements of climbing and inspection tasks. The advantages and disadvantages of typical CRs can be

© The Author(s), 2026. Published by Cambridge University Press.

https://doi.org/10.1017/S0263574726103580 Published online by Cambridge University Press

illustrated with the following: wheeled/tracked robots, for instance, must maintain constant adhesion to the wall and cannot perform obstacle-crossing functions; serial robots are limited by low load-bearing capacity; common PMs have the disadvantage of a relatively small workspace. In consideration of the limitations of existing CRs, this paper proposes a novel CR that features a kinematically redundant PM [15–17] as its core structure, integrated with a serial mechanism. Compared with the 3-RPR mechanism, this kinematically redundant PM exhibits a significantly larger workspace.

The objective of robot path planning is to find a feasible path from the starting point to the target point, and numerous path planning methods [18–22] have been proposed by scholars both domestically and internationally. Currently, research on trajectory planning for CRs mainly focuses on climbing experiments within the same plane or between two planes, with relatively limited studies on trajectory planning in three-dimensional environments, especially for parallel CRs. In path planning, CRs can be broadly classified into two categories: wheeled/tracked-based robots and legged robots. Trajectory planning for wheeled/tracked robots is relatively mature. For example, Luo et al. [23] proposed a method for wheeled robots to search for the optimal path in a two-dimensional space. Zhang et al. [24] studied the path planning for wheeled-based robots in uneven terrain. For legged CRs, since their motion does not follow a continuous path, the continuous paths need to be discretized into a series of discrete points, and the existing methods for wheel/track-based robots cannot be directly applied.

Common path planning algorithms are divided into global path planning and local path planning algorithms. The main goal of global path planning is to find the shortest path in the global environment. When a CR performs a task, it needs to cross different walls; it is necessary to analyze the transitions between walls before global path planning. Zhu et al. [25–27] have conducted transition analyses for trusses and walls in a 3D environment, and based on this research, they proposed an efficient three-layer framework method for path planning. Local path planning aims to search for the shortest collision-free path, and path planning in a single wall is relatively mature. For example, Zhang et al. [28] proposed a path planning algorithm based on Genetic Algorithm (GA) in a three-dimensional grid environment, which solves the problem of robots falling into a height trap. He et al. [29] conducted dynamic path planning based on an improved Artificial Potential Field Method (APF). In this study, the path search is divided into three layers: global path planning, local path planning, and single-step motion planning.

This paper introduces a novel CR featuring a kinematically redundant PM as its core structure, combined with a serial mechanism. To enhance the operational efficiency of CRs, path planning is conducted for the robots. The arrangement of the other parts of the paper is as follows: Section 2 analyzes the DOFs required for the PM and determines its configuration. Section 3 analyzes the position, velocity, singularity, and workspace of the PM. Section 4 is path planning for the CR, encompassing global path planning, local path planning, and single-step motion planning. Section 5 builds a physical prototype and conducts related experiments. Finally, Section 6 summarizes this paper.

2. Design of the climbing robot

2.1. Description of the robot structure

The structure of the proposed CR consists of the following modules, arranged from top to bottom: a replaceable tool module, an upper adsorption device, an upper rotating device, a kinematically redundant PM, a lower rotating device, and a lower adsorption device, as shown in Figure 1.

As shown in Figure 2, the kinematically redundant PM proposed in this paper essentially functions as a planar mechanism when the rotating devices are not considered. It consists of a moving platform, an intermediate platform, a fixed platform, and four RPR branches. The revolute joint axes of the mechanism are projected onto a common plane for simplified kinematic analysis. The centers of the R-joints attached to the fixed platform are designated as A_1, A_2, A_3, and A_4, all of which lie in the same horizontal plane. On the moving platform side, the R-joint axes of Branch 1 and Branch 2 coincide spatially. The projection of their intersection onto the simplified planar mechanism is defined as point P. Similarly,

https://doi.org/10.1017/S0263574726103580 Published online by Cambridge University Press

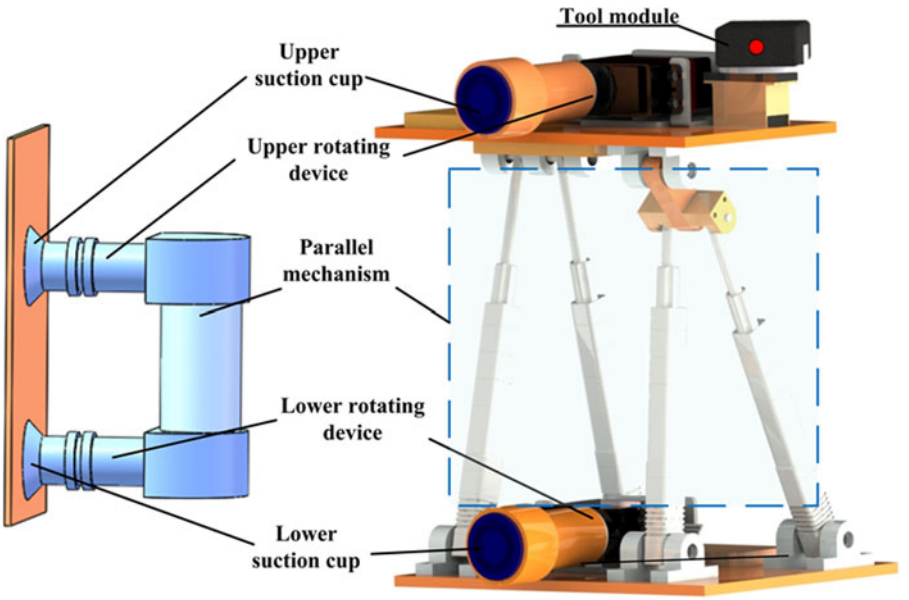


Figure 1. *Structure of the CR.*

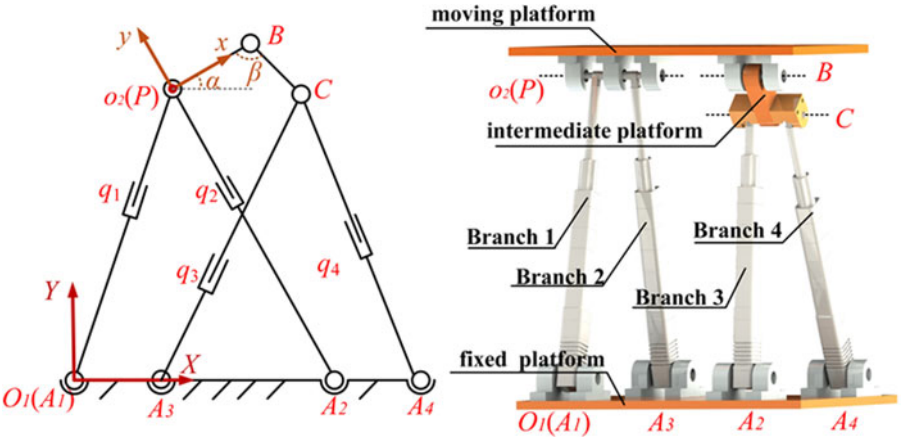


Figure 2. *Simplified diagram of the kinematically redundant PM.*

the coincident axes of Branch 3 and Branch 4 project to point C, while the intersection of the moving platform and the intermediate platform projects to point B.

In order to facilitate the subsequent analysis, a fixed coordinate frame O_1-XY is established at Point A_1, with the X-axis along the direction of A_1A_2 and the Y-axis perpendicular to A_1A_2, directed upwards. A moving coordinate frame o_2-xy is established at Point P, with the x-axis along the direction of PB and the y-axis perpendicular to PB, directed upwards. The distances from A_2, A_3, and A_4 to the Y-axis are denoted as l_2, l_3, and l_4, respectively, and their distances to the X-axis are zero. The length of PB is denoted as l_5, and the length of BC as l_6. The four prismatic joints serve as the driving joints of the mechanism, and the displacements of the prismatic joints are represented by q_i ($i = 1,2,3,4$).

2.2. Climbing process

The climbing process of the robot is illustrated in Figure 3. The fundamental gait cycle is as follows: In the initial state, both suction cups of the CR remain adhered to the wall surface. Subsequently, one

https://doi.org/10.1017/S0263574726103580 Published online by Cambridge University Press

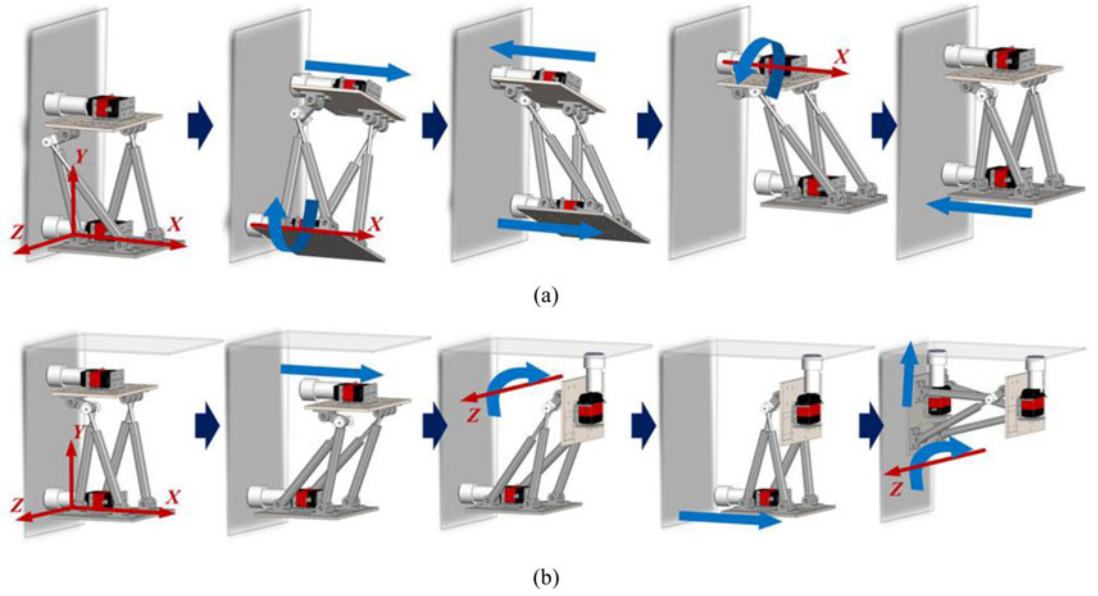


Figure 3. *Schematic of the robot climbing process: (a) Plane climbing gait; (b) Wall transition gait.*

suction cup releases its adhesion. Driven by the PM and the rotary device, the released end of the robot moves to a designated position, where the suction cup re-adheres. Then, the second suction cup releases its adhesion. Guided by the PM and the rotary device, this end subsequently moves to the second predefined position and re-adheres, completing one full climbing cycle.

This climbing process is categorized into two scenarios based on the working environment: (1) Plane climbing: As shown in Figure 3(a), the robot performs translational and rotational motions within a single wall surface. In this mode, the PM primarily adjusts the position, while the rotary devices adjust the orientation within the plane. (2) Wall transition: As shown in Figure 3(b), the robot traverses between two intersecting planes. This process requires the coordination of the PM and the rotary devices to rotate the robot's body around the intersection line, allowing the suction cups to align with the normal vector of the new surface.

2.3. Kinematically redundant PM DOF analysis

In order to determine the configuration of the CR, it is necessary to analyze the working environment of the CR. The CR requires the coordination of multiple DOFs for climbing on walls and transitioning between walls. During the climbing process, the translational DOF along the normal direction of the wall is denoted as TX, as shown in Figure 4(b). The direction perpendicular to the wall normal and pointing upwards is denoted as TY, as shown in Figure 4(c). The rotation DOF along the wall normal direction is denoted as RX, as shown in Figure 4(d). Therefore, through the coordination of these three DOFs, motion within a single wall surface can be achieved. For transitioning between walls, an additional rotation DOF denoted as RZ is required, as shown in Figure 4(e).

Through the above analysis, it is determined that the CR requires a minimum of four DOFs to achieve the climbing task. Conventional 2T2R PMs, due to their structural limitations, cannot be directly applied to CR. For example, a 2-RPU/2-SPU PM [30] possesses two translational DOFs: one along the normal direction of the moving platform and the other along the radial direction of the revolute joints on the fixed platform, as well as two rotational DOFs about the two axes of the universal joint on the moving platform. The mechanism is structurally complex, and the branch assembly requirements are high. The fixed platform size of the 2PRS/2PUS mechanism [31] is large, which is suitable for scenarios such as machine tools. 2UPU&R (2R (RR&RPR)R) [32] is complex in structure and large in size, which is not suitable for CRs.

https://doi.org/10.1017/S0263574726103580 Published online by Cambridge University Press

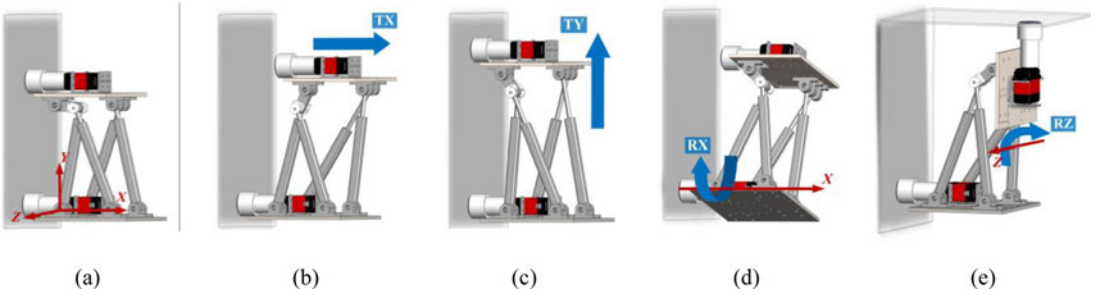


Figure 4. *The minimum DOFs required for a CR: (a) Climbing environment 1; (b) Translational DOF TX; (c) Translational DOF TY; (d) Rotational DOF RX; (e) Climbing environment 2 and rotational DOF RZ.*

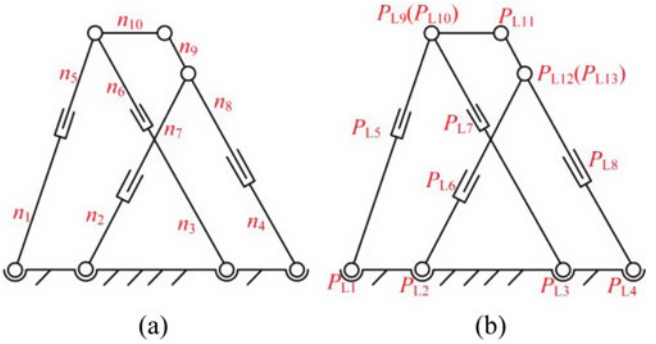


Figure 5. *Kinematic diagram of the PM for DOF analysis:(a) Identification of the 10 movable links (n_1–n_{10}); (b) Distribution of the 13 lower kinematic pairs (P_{L1}–P_{L13}).*

Therefore, the required four DOFs are decomposed into two parts: the rotational DOF RX is provided by the serial rotary device, while the remaining DOFs can be achieved using a 3-RPR PM. However, the RZ rotational capability of this mechanism is highly limited and insufficient for wall-climbing applications that require the robot to traverse right-angle or acute-angle wall transitions. Such maneuvers typically demand at least 90° of rotation in RZ, which exceeds the range a conventional 3-RPR PM can provide [33]. To overcome this limitation and expand the rotational workspace, an intermediate platform and an additional RPR branch are introduced. This modification effectively upgrades the system into a kinematically redundant PM, as shown in Figure 2.

Based on the previous description, the aforementioned PM is a planar mechanism. According to the DOF formula [34] for planar mechanisms, its mobility can be calculated as follows:

$$F = 3n - 2P_L - P_H = 4 \tag{1}$$

where: n denotes the number of movable links in the mechanism, P_L represents the number of lower pairs, and P_H indicates the number of higher pairs.

In the mechanism under discussion, the specific identification of these components is illustrated in Figure 5. Specifically, Figure 5(a) labels the ten movable links as n_i ($n = 10$), while Figure 5(b) denotes the thirteen lower kinematic pairs as P_{Lj} ($P_L = 13$). There are no higher pairs in this configuration ($P_H = 0$).

In summary, the mechanism possesses four DOFs. Due to its inherent planar nature, the moving platform contributes only three DOFs within the plane. The mechanism is actuated by four actuators, which match the total DOFs of the system but exceed the number of DOFs exhibited by the moving platform. Therefore, this configuration should be categorized as a kinematically redundant PM.

https://doi.org/10.1017/S0263574726103580 Published online by Cambridge University Press

3. Kinematics analysis

3.1. Position analysis

3.1.1. Inverse kinematics analysis

Inverse kinematics is the process of determining the required actuator variables to achieve a specific pose of the end-effector. In the context of the proposed kinematically redundant PM, this problem specifically involves calculating the linear displacements of the four prismatic driving joints, denoted as q_i ($i = 1, 2, 3, 4$). The inputs for this calculation are the position of the reference point p on the moving platform (represented by coordinates x, y), the orientation of the moving platform (α), and the angle of the intermediate platform (β), as explicitly identified in Figure 2.

Based on the coordinate frame established in the previous section, the position vector of point p in the fixed coordinate frame O_1-XY can be obtained as:

$$\mathbf{p} = \begin{bmatrix} x & y \end{bmatrix}^{\mathrm{T}} \tag{2}$$

Similarly, the position vectors of points A_i ($i = 1,2,3,4$) in the fixed coordinate frame are:

$$\begin{cases} \boldsymbol{a}_1 = \begin{bmatrix} 0 & 0 \end{bmatrix}^{\mathrm{T}} \\ \boldsymbol{a}_2 = \begin{bmatrix} l_2 & 0 \end{bmatrix}^{\mathrm{T}} \\ \boldsymbol{a}_3 = \begin{bmatrix} l_3 & 0 \end{bmatrix}^{\mathrm{T}} \\ \boldsymbol{a}_4 = \begin{bmatrix} l_4 & 0 \end{bmatrix}^{\mathrm{T}} \end{cases} \tag{3}$$

The position vectors of points B and C in the moving coordinate frame o_2-xy are denoted as:

$$\boldsymbol{b}^{o_2} = \begin{bmatrix} l_5 & 0 \end{bmatrix}^{\mathrm{T}} \tag{4}$$

$$\boldsymbol{c}^{o_2} = \boldsymbol{b}^{o_2} + \boldsymbol{R}_f \begin{bmatrix} l_6 & 0 \end{bmatrix}^{\mathrm{T}} \tag{5}$$

Where: $\boldsymbol{R}_f = \begin{bmatrix} \cos\beta & -\sin\beta \\ \sin\beta & \cos\beta \end{bmatrix}$, β represents the angle between the moving platform and the intermediate platform.

The position vectors of points B and C in the fixed coordinate frame can be represented as:

$$\boldsymbol{b} = \boldsymbol{p} + \boldsymbol{R}\boldsymbol{b}^{o_2} \tag{6}$$

$$\boldsymbol{c} = \boldsymbol{b} + \boldsymbol{R}\boldsymbol{R}_f \begin{bmatrix} l_6 & 0 \end{bmatrix}^{\mathrm{T}} \tag{7}$$

Where: $\boldsymbol{R} = \begin{bmatrix} \cos\alpha & -\sin\alpha \\ \sin\alpha & \cos\alpha \end{bmatrix}$, α represents the angle of rotation of the moving platform around the Z-axis.

For branches 1 and 2, the constraint equations for the limbs are expressed as:

$$q_i^2 = (\boldsymbol{p} - \boldsymbol{a}_i)^{\mathrm{T}}(\boldsymbol{p} - \boldsymbol{a}_i), (i = 1, 2) \tag{8}$$

Similarly, for branches 3 and 4, the constraint equations are established as:

$$q_i^2 = (\boldsymbol{c} - \boldsymbol{a}_i)^{\mathrm{T}}(\boldsymbol{c} - \boldsymbol{a}_i), (i = 3, 4) \tag{9}$$

Based on Eqs. (8) and (9), the inverse position solution of the mechanism is obtained as follows:

$$\begin{cases} q_1 = \sqrt{x^2 + y^2} \\ q_2 = \sqrt{(x - l_2)^2 + y^2} \\ q_3 = \sqrt{(y + e_1)^2 + (e_2 - x)^2} \\ q_4 = \sqrt{(y + e_1)^2 + (e_3 - x)^2} \end{cases} \tag{10}$$

Where: $e_1 = \mathrm{s}_\alpha(l_5 + l_6 c_\beta) + l_6 c_\alpha s_\beta$, $e_2 = l_3 - c_\alpha(l_5 + l_6 c_\beta) + l_6 s_\alpha s_\beta$, $e_3 = l_4 - c_\alpha(l_5 + l_6 c_\beta) + l_6 s_\alpha s_\beta$.

https://doi.org/10.1017/S0263574726103580 Published online by Cambridge University Press

Since this mechanism is a kinematically redundant PM, if only the position and orientation of the moving platform are given, the inverse positions of branches 1 and 2 are uniquely determined, but the inverse positions of branches 3 and 4 are not unique. This is due to the existence of multiple possible values for the β angle between the moving platform and the intermediate platform, leading to a multitude of inverse positions of branches 3 and 4. Consequently, to uniquely determine the inverse kinematics solutions for branches 3 and 4, the β angle must be specified.

3.1.2. Forward kinematics analysis

The forward kinematics problem involves solving for the position and orientation of the moving platform and the angle between the moving platform and the intermediate platform using the driving values q_i of the branches. Based on the first two equations in Eq. (10), the position of the moving platform can be derived as:

$$\mathbf{p} = \begin{bmatrix} p_x \\ p_y \end{bmatrix} = \begin{bmatrix} \dfrac{{q_2}^2 - {q_1}^2 - {l_2}^2}{-2l_2} \\ \sqrt{{q_1}^2 - \left(\dfrac{{q_2}^2 - {q_1}^2 - {l_2}^2}{-2l_2}\right)^2} \end{bmatrix} \tag{11}$$

Combined with Eq. (7) and the latter two equations in Eq. (10), the position vector of point C in the O_1-XY frame can be expressed as:

$$\mathbf{c} = \begin{bmatrix} c_x \\ c_y \end{bmatrix} = \begin{bmatrix} \dfrac{q_4^2 - q_3^2 + l_3^2 - l_4^2}{2(l_3 - l_4)} \\ \sqrt{q_3^2 - \left(l_3 - \dfrac{q_4^2 - q_3^2 + l_3^2 - l_4^2}{2(l_3 - l_4)}\right)^2} \end{bmatrix} \tag{12}$$

Let k denote the distance between points p and C:

$$k = \overline{pc} = \sqrt{(p_x - c_x)^2 + (p_y - c_y)^2} \tag{13}$$

Using triangle PBC, angle β can be expressed as:

$$\beta = -\left(\pi - \arccos\left(\frac{{l_5}^2 + {l_6}^2 - k^2}{2l_5 l_6}\right)\right) \tag{14}$$

Let θ_1 denote the angle between PB and PC, and θ_2 denote the angle between PC and the X-axis. Both angles can be expressed as:

$$\begin{cases} \theta_1 = \arccos\left(\dfrac{l_5^2 + k^2 - l_6^2}{2l_5 k}\right) \\ \theta_2 = \arctan\left(\dfrac{c_y - p_y}{c_x - p_x}\right) \end{cases} \tag{15}$$

Angle α can be expressed as:

$$\alpha = \theta_1 + \theta_2 \tag{16}$$

The forward kinematics of the PM can be solved using Eqs. (11), (14), and (16).

3.2. Velocity and singularity analysis

Velocity analysis is the foundation for subsequent singularity and workspace analysis. In the subsequent analysis, the velocity $\boldsymbol{v}_p$ at the point P, the angular velocity of the moving platform with respect to the Z-axis $\dot{\alpha}$ and the relative angular velocity of the moving platform to the intermediate platform are $\dot{\beta}$ known.

https://doi.org/10.1017/S0263574726103580 Published online by Cambridge University Press

3.2.1. Jacobian matrix analysis

The Jacobian matrix of PM plays an important role in singular position analysis, so it is necessary to analyze the Jacobian matrix of this mechanism [16].

In branches 1 and 2, differentiating Eq. (8) with respect to time gives:

$$q_i\dot{q}_i = (\boldsymbol{p} - \boldsymbol{a}_i)^{\mathrm{T}}\dot{\boldsymbol{p}}, (i = 1, 2) \tag{17}$$

Similarly, in branches 3 and 4, differentiating Eq. (9) with respect to time gives:

$$q_i\dot{q}_i = (\boldsymbol{c} - \boldsymbol{a}_i)^{\mathrm{T}}\dot{\boldsymbol{c}}, (i = 3, 4) \tag{18}$$

The constraint equation for the intermediate platform BC can be expressed as follows:

$$l_6^2 = (\boldsymbol{c} - \boldsymbol{b})^{\mathrm{T}}(\boldsymbol{c} - \boldsymbol{b}) \tag{19}$$

Taking the derivative of Eq. (19) with respect to time, we obtain:

$$(\boldsymbol{c} - \boldsymbol{b})^{\mathrm{T}}\dot{\boldsymbol{b}} = (\boldsymbol{c} - \boldsymbol{b})^{\mathrm{T}}\dot{\boldsymbol{c}} \tag{20}$$

By rearranging Eq. (18), we can obtain:

$$\boldsymbol{G}\dot{\boldsymbol{c}} = \boldsymbol{H} \tag{21}$$

Where: $\boldsymbol{G} = \begin{bmatrix}(\boldsymbol{c} - \boldsymbol{a}_3)^{\mathrm{T}} \\ (\boldsymbol{c} - \boldsymbol{a}_4)^{\mathrm{T}}\end{bmatrix}, \boldsymbol{H} = \begin{bmatrix}q_3\dot{q}_3 \\ q_4\dot{q}_4\end{bmatrix}$.

For the matrix $\boldsymbol{G}$, as long as branches 3 and 4 do not coincide (i.e., $l_3 \neq l_4$), the matrix remains full-rank. Therefore, Eq. (21) can be rearranged to obtain:

$$\dot{\boldsymbol{c}} = \boldsymbol{K}\boldsymbol{H} \tag{22}$$

Where: $\boldsymbol{K} = \frac{1}{(\boldsymbol{c}-\boldsymbol{a}_3)^{\mathrm{T}}\boldsymbol{L}(\boldsymbol{c}-\boldsymbol{a}_4)}\left[\boldsymbol{L}(\boldsymbol{c} - \boldsymbol{a}_4) \ -\boldsymbol{L}(\boldsymbol{c} - \boldsymbol{a}_3)\right], \boldsymbol{L} = \begin{bmatrix}0 & -1 \\ 1 & 0\end{bmatrix}$.

By taking the derivative of Eq. (6) with respect to time and substituting it along with Eq. (22) into Eq. (20), we obtain:

$$(\boldsymbol{c} - \boldsymbol{b})^{\mathrm{T}}\left(\dot{\boldsymbol{p}} + \dot{\alpha}\boldsymbol{L}\boldsymbol{R}\boldsymbol{b}^{o_2}\right) = (\boldsymbol{c} - \boldsymbol{b})^{\mathrm{T}}\boldsymbol{K}\boldsymbol{H} \tag{23}$$

Based on the analysis in the previous section, the moving platform has three DOFs (2T1R). The velocity of the moving platform is defined as $\boldsymbol{t}_p = [\dot{x} \ \ \dot{y} \ \ \dot{\alpha}]^{\mathrm{T}}$, and the velocity of the driving joint is defined as $\dot{\boldsymbol{q}} = [\dot{q}_1 \ \ \dot{q}_2 \ \ \dot{q}_3 \ \ \dot{q}_4]^{\mathrm{T}}$.

Therefore, rearranging Eqs. (17) and (23) we obtain:

$$\boldsymbol{J}_A\boldsymbol{t}_p = \boldsymbol{J}_q\dot{\boldsymbol{q}}_i \tag{24}$$

Where: $\boldsymbol{J}_A = \begin{bmatrix}(\boldsymbol{p} - \boldsymbol{a}_1)^{\mathrm{T}} & 0 \\ (\boldsymbol{p} - \boldsymbol{a}_2)^{\mathrm{T}} & 0 \\ (\boldsymbol{b} - \boldsymbol{c})^{\mathrm{T}} & (\boldsymbol{b} - \boldsymbol{c})^{\mathrm{T}}\boldsymbol{L}\boldsymbol{R}\boldsymbol{b}^{o_2}\end{bmatrix}_{3\times3}, \boldsymbol{J}_q = \begin{bmatrix}q_1 & 0 & 0 & 0 \\ 0 & q_2 & 0 & 0 \\ 0 & 0 & \boldsymbol{n}_1 & \boldsymbol{n}_2\end{bmatrix}_{3\times4}, \boldsymbol{n}_1 = \dfrac{(\boldsymbol{c} - \boldsymbol{b})^{\mathrm{T}}\boldsymbol{L}(\boldsymbol{c} - \boldsymbol{a}_4)q_3}{(\boldsymbol{c} - \boldsymbol{a}_3)^{\mathrm{T}}\boldsymbol{L}(\boldsymbol{c} - \boldsymbol{a}_4)}$,

$\boldsymbol{n}_2 = \dfrac{-(\boldsymbol{c} - \boldsymbol{b})^{\mathrm{T}}\boldsymbol{L}(\boldsymbol{c} - \boldsymbol{a}_3)q_4}{(\boldsymbol{c} - \boldsymbol{a}_3)^{\mathrm{T}}\boldsymbol{L}(\boldsymbol{c} - \boldsymbol{a}_4)}$.

3.2.2 Velocity analysis

Since the angular velocity is perpendicular to the XOY plane, subsequent analysis and calculations need to be conducted in a three-dimensional space. For the coordinate frame established in the previous section, all points have zero linear velocity components in the Z-axis direction. Therefore, the position vector of point p can be represented as $\boldsymbol{p} = [x \ \ y \ \ 0]^{\mathrm{T}}$, and the position vectors of other points can be transformed into three-dimensional vectors using the same method as for point P.

https://doi.org/10.1017/S0263574726103580 Published online by Cambridge University Press

Therefore, the velocity of point p is represented as:

$$\boldsymbol{V}_p = \begin{bmatrix} \boldsymbol{v}_p \\ \boldsymbol{\omega}_p \end{bmatrix} = \begin{bmatrix} \begin{bmatrix} \dot{x} & \dot{y} & 0 \end{bmatrix}^{\mathrm{T}} \\ \begin{bmatrix} 0 & 0 & \dot{\alpha} \end{bmatrix}^{\mathrm{T}} \end{bmatrix} \tag{25}$$

Similarly, the velocity of point B is:

$$\boldsymbol{V}_b = \begin{bmatrix} \boldsymbol{v}_b \\ \boldsymbol{\omega}_b \end{bmatrix} = \begin{bmatrix} \boldsymbol{v}_p + \boldsymbol{\omega}_p \times \boldsymbol{s}_b \\ \boldsymbol{\omega}_p \end{bmatrix} \tag{26}$$

Where: $\boldsymbol{s}_b$ represents the vector from the point p to the point B in a fixed coordinate system.

The linear velocity of the point P can be expressed in another way, as Eq. (27):

$$\boldsymbol{v}_p = \dot{q}_i \boldsymbol{l}_i + \boldsymbol{\omega}_{li} \times (q_i \cdot \boldsymbol{l}_i), (i = 1, 2) \tag{27}$$

Where: $\boldsymbol{l}_i$ represents the unit vector from A_i to P, $\boldsymbol{\omega}_{li}$ denotes the angular velocities of the driving joints.

By multiplying both sides of Eq. (27) by $\boldsymbol{l}_i$, we can derive the velocity of the driving joints 1 and 2 as:

$$\dot{q}_i = \boldsymbol{l}_i^T \boldsymbol{v}_p, (i = 1, 2) \tag{28}$$

In order to determine the angular velocities of parts in branches 1 and 2, we perform a cross product with $\boldsymbol{l}_i$ on both sides of the Eq.(27), and the following angular velocity expression is obtained:

$$\boldsymbol{\omega}_{li} = \frac{\boldsymbol{l}_i \times \boldsymbol{v}_p}{q_i}, (i = 1, 2) \tag{29}$$

For branches 3 and 4, the linear velocity of the point C can be expressed as shown in Eq. (30). Alternatively, it can be formulated in a different way as demonstrated in Eq. (31):

$$\boldsymbol{v}_c = \boldsymbol{v}_b + \boldsymbol{\omega}_c \times \boldsymbol{s}_c \tag{30}$$

$$\boldsymbol{v}_c = \dot{q}_i \boldsymbol{l}_i + \boldsymbol{\omega}_{li} \times (q_i \cdot \boldsymbol{l}_i), (i = 3, 4) \tag{31}$$

Where: $\boldsymbol{s}_c$ represents the vector from the point B to the point C in a fixed coordinate system, $\boldsymbol{l}_i$ represents the unit vector from A_i to C.

Similarly, the velocities of the driving joints 3 and 4 can be represented as:

$$\dot{q}_i = \boldsymbol{l}_i^T \boldsymbol{v}_c, (i = 3, 4) \tag{32}$$

The angular velocities of parts in branches 3 and 4 are represented as:

$$\boldsymbol{\omega}_{li} = \frac{\boldsymbol{l}_i \times \boldsymbol{v}_c}{q_i}, (i = 3, 4) \tag{33}$$

3.3. Singularity analysis

When the mechanism is in a singular position, there is a significant alteration in its motion accuracy, stability, and DOFs. For example, instantaneous changes in the number of DOFs can cause the mechanism to jam, result in mechanical structure damage, or lead to loss of control. Therefore, studying the singularity of the mechanism can help us identify its singular configuration and ensure the safe operation of the mechanism.

The singular configurations of a mechanism can be obtained by analyzing the rank of the Jacobian matrix of Eq. (24). When the rank of the matrix $\boldsymbol{J}_q$ is reduced, inverse kinematic singularity occurs in the mechanism; When the rank of the matrix $\boldsymbol{J}_A$ is reduced, forward kinematic singularity occurs; When the ranks of both matrices are reduced, mixed singularity occurs in the mechanism [35, 36].

https://doi.org/10.1017/S0263574726103580 Published online by Cambridge University Press

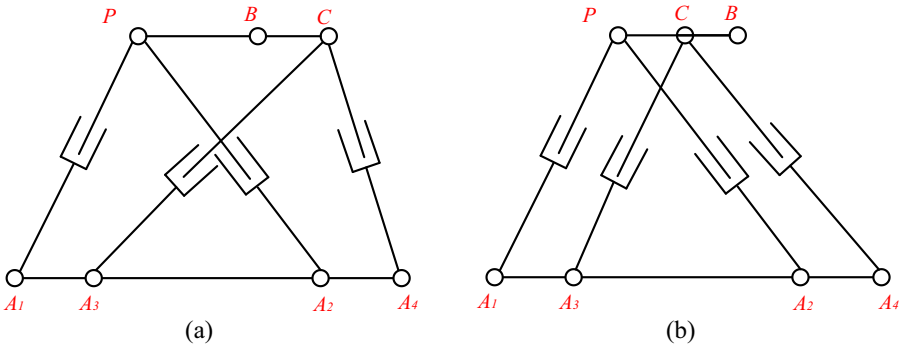


Figure 6. *Singular configurations: (a) Singular configuration 1; (b) Singular configuration 2.*

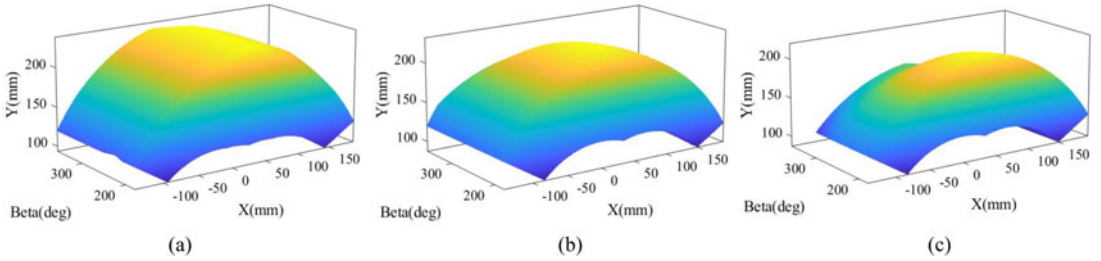


Figure 7. *Workspace of the PM: (a) $\alpha = 0°$; (b) $\alpha = 45°$; (c) $\alpha = 90°$.*

According to the Jacobian matrix, the rows within matrix $\boldsymbol{J}_A$ correspond to the position vectors of PA_1, PA_2, and BC; these position vectors are non-zero. In the design process, as long as the positions of points A_1 and A_2 do not coincide, PA_1 and PA_2 will not be collinear. Since PA_1 and PA_2 intersect at point P, it is necessary to ensure that BC and PB are not collinear to prevent forward kinematic singularity. In matrix $\boldsymbol{J}_q$, the displacement of the driving joints q_i ($i = 1, 2, 3, 4$) will not be zero. Therefore, it is only necessary to analyze the position vectors of CA_3 and CA_4 when the positions of A_3 and A_4 do not coincide; inverse kinematic singularity will not occur, a condition that can be avoided during the design process. Through the above analysis, some singularities of the mechanism can be avoided through structural design. Therefore, during the operation of the mechanism, forward kinematic singularity will occur when BC and PB are collinear; the mechanism will have no forward kinematic singularity and mixed singularity. The robot must avoid entering these singular configurations during movement, as shown in Figure 6.

3.4. Workspace analysis

The reachable workspace [37, 38] of a PM refers to all the positions and orientations that the moving platform can reach under corresponding constraints. The solution of the workspace of the PM is based on the inverse kinematics of the PM, which is solved by the numerical search method, as shown in Figure 7. The parameters of the mechanism are as follows: $l_2 = 68$ mm, $l_3 = 0$, $l_4 = 68$ mm, $l_5 = 43$ mm, $l_6 = 25$ mm, the motion range for driving q_i ($i = 1, 2, 3, 4$) is $120 \sim 240$ mm, the range of β angle is $180° \sim 360°$, the angular range of the joints is $-50° \sim 50°$.

The figure presents the workspace for α angles of 0°, 45°, and 90°, and it can be seen from the figure that as the α angle increases, the workspace of the mechanism gradually decreases in the y-axis direction. When the CR is in motion, the poses of the upper and lower adsorption devices relative to the upper and lower platforms remain constant; only simple coordinate transformations are needed, which will not be further elaborated here.

https://doi.org/10.1017/S0263574726103580 Published online by Cambridge University Press

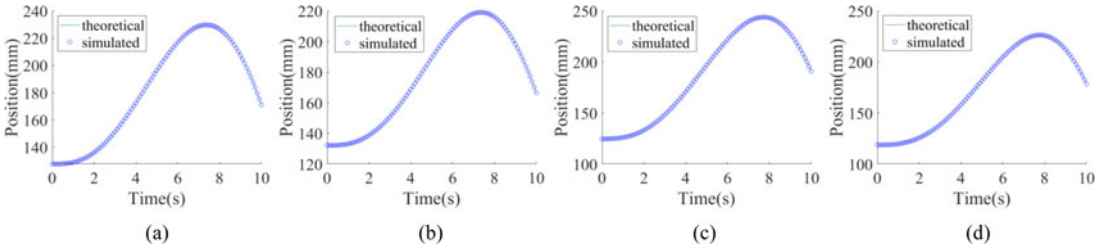


Figure 8. *Comparison between theoretical and simulated values for position analysis: (a) drive joint 1; (b) drive joint 2; (c) drive joint 3; (d) drive joint 4.*

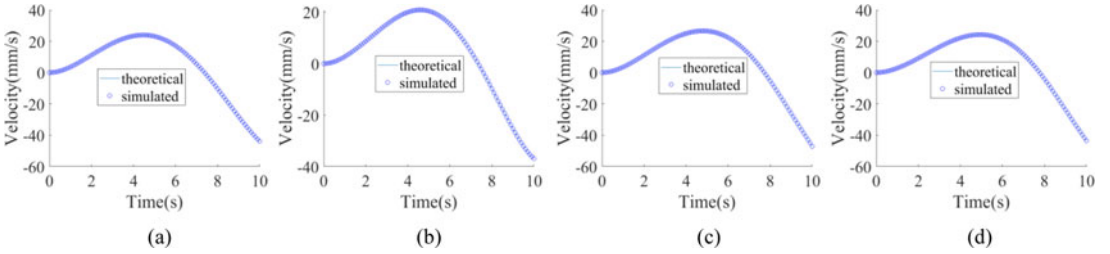


Figure 9. *Comparison between theoretical and simulated values for velocity analysis: (a) drive joint 1; (b) drive joint 2; (c) drive joint 3; (d) drive joint 4.*

3.5. Simulation

After conducting the aforementioned analysis, the kinematics of the PM were simulated, encompassing both position and velocity simulations. The trajectory of a moving platform is defined as:

$$\begin{cases} \alpha = -\dfrac{\pi}{180}\left(45\dfrac{t^5}{10000} - 25\dfrac{t^4}{400} + 9\dfrac{t^3}{80}\right) \\ \beta = \dfrac{\pi}{180}\left(9\dfrac{t^5}{10000} - 9\dfrac{t^4}{400} + 3\dfrac{t^3}{20}\right) + 11\dfrac{\pi}{9} \\ x = \left(8\dfrac{t^5}{2500} - 9\dfrac{t^4}{100} + 3\dfrac{t^3}{5}\right) + 25 \\ y = \left(21\dfrac{t^5}{2500} - 22\dfrac{t^4}{100} + 7\dfrac{t^3}{5}\right) + 125 \end{cases} \quad (t = 0 \sim 10s) \tag{34}$$

The simulation results for inverse position and velocity are shown in Figures 8 and 9, respectively. The simulated values are represented by circles, while the theoretical values are depicted by solid lines. Upon comparison, the data from the theoretical and simulated values align well, verifying the correctness of the kinematic modeling.

4. Path planning

Path planning is the process of calculating one or more effective paths from a starting point to a target point. In complex three-dimensional environments, to quickly find the optimal effective path, the path search is divided into three layers for layer-by-layer processing, enabling the rapid search of a shortest path that avoids obstacles and is free from singularities [26]. The three-level framework consists of global path planning, local path planning, and single-step motion planning.

https://doi.org/10.1017/S0263574726103580 Published online by Cambridge University Press

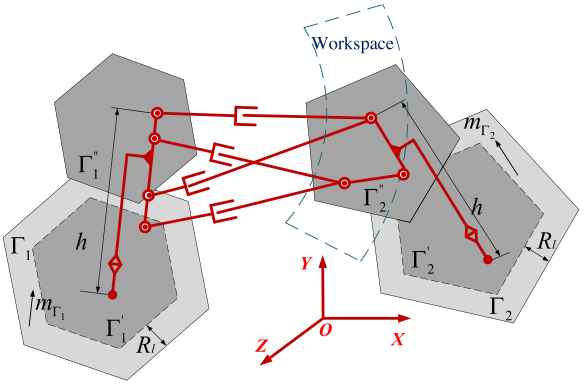


Figure 10. *Simplified model of walls and CR.*

4.1. Global path planning

Before conducting global path planning, the transitional capability between two walls for the CR must be analyzed. If the suction cup at one end of the robot is anchored within a plane, and the robot's workspace intersects with another plane, then the inter-wall transition is deemed feasible. In order to quickly analyze the transition between wall surfaces, the model is simplified as shown in Figure 10. For ease of representation and subsequent analysis, we define a method for representing walls in a three-dimensional environment. The coordinates of wall vertices are expressed in the base coordinate system as follows:

$$D_i = \{P | P \in \Gamma_i\} \tag{35}$$

Where: D_i denotes the vertices of the wall surface, Γ_i denotes the wall surface. The normal vector of the wall surface is denoted as $\boldsymbol{m}$, which can be calculated using the coordinates of the wall vertices.

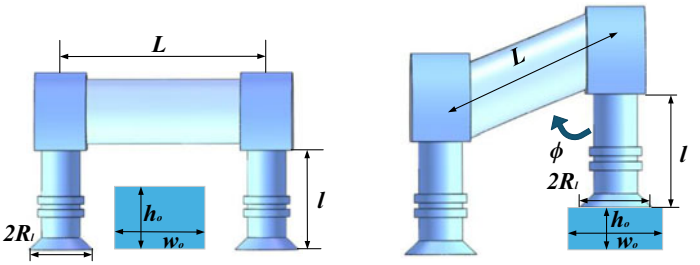
To ensure that the entire adsorption area of the suction cup lies within the wall surface, the wall surface is contracted inwards by a distance of R_l (the radius of the suction cup). The position of the suction cup on the wall surface can be simplified to a point (the geometric center of the suction contact area). When the suction cup is securely adhered to the wall surface, the normal of the suction surface, the axis of the rotating device, and the normal of the wall surface are parallel to each other, so the inwardly retracted walls are moved a distance of h along the normal direction of the walls. The wall surfaces in contact with the adsorption devices on the fixed and moving platform sides are denoted as Γ_1 and Γ_2, respectively; their corresponding point-simplified versions are designated as Γ_1' and Γ_2'; and the surfaces mapped onto the fixed and moving platforms of PM are referred to as Γ_1'' and Γ_2'', respectively.

If a transition is possible between the two walls, after translation, the coordinate origins of the upper and lower platforms of the PM will be respectively positioned within these two walls. The rotation range of the moving platform in the PM is from $-20°$ to $110°$, and it can achieve climbing on walls with large angles. After simplified modeling, taking a point on one of the simplified wall surfaces as the coordinate origin, if the workspace of the PM intersects with the other wall plane, it indicates the feasibility of inter-wall traversal between the two surfaces.

During the search process, the wall surfaces in the environment are first assigned numerical labels. Subsequently, the transitions between each pair of wall surfaces are analyzed. Specifically, transition analysis is performed on point pairs near the boundary regions of two wall surfaces. The results of this analysis are stored in the adjacency matrix. The adjacency matrix is a square matrix used to represent the connection relationships between vertices in the graph.

Following the transitional feasibility analysis, the wall surface at the starting point is designated as the root node. The tree is then traversed in a depth-first manner, visiting all wall surfaces until a leaf node is reached. The search then backtracks to the previous wall surface and continues searching along other branches, until all possible wall paths from the starting wall surface to the target wall surface are identified.

https://doi.org/10.1017/S0263574726103580 Published online by Cambridge University Press



(a) (b)

Figure 11. *Obstacle analysis: (a) step over obstacles (b) step on obstacles.*

For each accessible wall path, the transition point pairs are computed in a pairwise manner according to the path sequence. During the computation of transition point pairs, the robotic constraint equations (e.g., Eq. (36)) are incorporated. If a point pair satisfies the constraints, it is stored as a candidate transition point pair. After solving for the candidate transition point pairs, we optimize the selection of transition points to minimize the total global path length. The global path solution equation is presented as Eq. (37).

$$\begin{cases} \boldsymbol{q} = IK(x, y, \alpha, \beta) \\ \boldsymbol{J}_A \neq 0 \\ \boldsymbol{P}_i^S \in \Gamma_{i+1} \\ \boldsymbol{P}_i^E \in \Gamma_i \end{cases} \tag{36}$$

$$\boldsymbol{P}_{\min}(x, y, z) = \sum_{i=1}^{N} \left| \boldsymbol{P}_i^E - \boldsymbol{P}_i^S \right| + \sum_{i=1}^{N-1} \left| \boldsymbol{P}_{i+1}^B - \boldsymbol{P}_i^B \right| \tag{37}$$

where: N represents the number of walls, $\boldsymbol{P}_i^S$ and $\boldsymbol{P}_i^E$ denote the coordinate positions of the transition points within the wall surfaces, $\boldsymbol{IK}$ represents the inverse kinematic of the PM, $\boldsymbol{q}$ represents the displacements of the driving joints in the PM, $\boldsymbol{q} = [q_1, q_2, q_3, q_4]$, and Γ_i denotes the i-th wall. $\boldsymbol{J}_A$ denotes the Jacobian matrix.

4.2. Local path planning and Single-step motion planning

In the previous section, the globally shortest path was identified, but the path within the wall surfaces has not yet been processed. On the wall surfaces, there exist obstacles of different sizes, and different strategies are adopted for these obstacles. Therefore, a cost function is incorporated into the original A^* algorithm [39] to handle various obstacles. The obstacles on the walls are classified according to the robot's movement capabilities, with step over obstacles and step on obstacles illustrated in Figure 11(a) and (b).

Based on the three-dimensional dimensions of the obstacles, for those that can be stepped over, their length can be disregarded, while their width and height dimensions should meet the following conditions:

$$\begin{cases} w_o \leq L - 2R_l \\ h_o \leq l \end{cases} \tag{38}$$

Where: w_o and h_o indicate the length and height of the obstacle, respectively. R_l is the radius of the suction cup, L represents the robot's maximum movement range, and l denotes the distance between the lowest point of the connecting rod in a PM and the adsorption surface of the suction cup.

https://doi.org/10.1017/S0263574726103580 Published online by Cambridge University Press

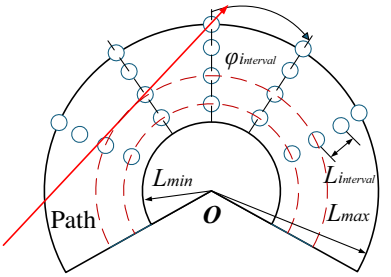


Figure 12. *Schematic diagram for solving discrete points.*

For the case that can step on an obstacle, the dimensions of the obstacle should meet the following constraints:

$$\begin{cases} w_o \geq 2R_l \\ l_o \geq 2R_l \\ h_o \leq L\cos\phi \end{cases} \tag{39}$$

where: ϕ denotes the rotation angle at the joint, and l_o denotes the length of the obstacle.

For obstacles of other sizes, the CR can only choose to bypass them. The improved A^* algorithm is shown in Eq. (40):

$$f(u) = g(u) + h(u) + o(u) \tag{40}$$

where: $g(u)$ represents the actual distance to the goal point, $h(u)$ represents the Manhattan distance to the goal point, $o(u)$ represents the cost function, and is used to deal with different obstacles. For obstacles that require detouring, their cost function is set to infinity. For traversable or step on obstacles, their cost function is determined by multiplying the obstacle's height by a coefficient(k^*h_o).

The path searched by the improved A* algorithm is continuous, whereas the movement of the CR is in a discrete point-to-point form; therefore, the path needs to be discretized. During the discretization process, since the rotating device of the CR can rotate 240°, an annular sector region is formed, centered at the starting point with a radius equivalent to CR's motion range, as illustrated in Figure 12. The extent of this region can be mathematically described by Eq. (41).

The path points within the annular region can be considered as potential discrete points. If a potential discrete point intersects with the path, it is designated as a discrete point. If there are multiple intersects within the annular region, the point nearest to the target position should be selected as the discrete point while avoiding obstacles. Then, this discrete point is taken as the new starting point, and the above operations are repeated. If there are no path points within the annular area, the range of the annular area is adjusted, and the search is redone. Finally, to ensure safety, collision detection is performed on the above discrete points.

$$\begin{cases} x_a = x_0 + (L_{\max} - L_{\min}) \cdot \sin\varphi \\ y_a = y_0 + (L_{\max} - L_{\min}) \cdot \cos\varphi \\ z_a = z_0 \end{cases} \tag{41}$$

Where: $[x_a\ y_a\ z_a]$ represents the coordinates of potential discrete points within the region, $[x_0\ y_0\ z_0]$ denotes the coordinates of the current point, and φ indicates the rotation angle.

Through the search process outlined above, we obtain all the discrete points from the starting point to the target point.

4.3. Simulation

After a theoretical analysis, each layer of the three-layer search framework was simulated, including global path planning, local path planning, and collision-free, singularity-free single-step motion.

https://doi.org/10.1017/S0263574726103580 Published online by Cambridge University Press

Table 1. *Global path search time and length*

Number of walls	2	3	4	5	6
Average time/s	1.59	2.76	3.93	5.10	6.09
Average length/mm	913.85	1,254.25	1643.57	2,420.66	2,824.01

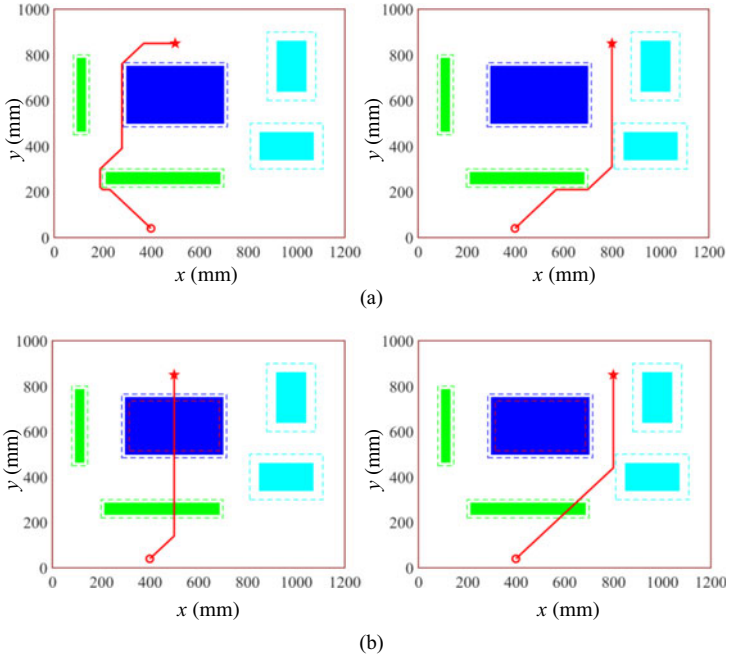


Figure 13. *Comparison of path search between the traditional A* algorithm and the improved A* algorithm: (a) traditional A* algorithm (b) improved A* algorithm.*

4.3.1 Global path planning simulation

In Global Path Planning, a given set of 50 sets of walls (number of walls is 2–6) is analyzed using the Global Path Planner. During global path planning experiments, 50 sets of planes (each containing 2–6 planes) were analyzed. To optimize computational efficiency, the mechanism workspace was precomputed offline. The number of transition point pairs sampled within each wall was set to 100. The total search time for all transition point pairs remained approximately 6 s, with search time increasing proportionally as the number of walls (planes) grew. Table I lists the search time and path length.

4.3.2 Local path planning simulation

During the local path-finding process, a local path search within the plane was conducted for 50 sets of walls from the global path planning. Taking two of these groups as examples, the results are shown in Figure 13. In the figure, obstacles are differentiated by color: green denotes traversable obstacles, blue indicates obstacles that can be stepped on, and cyan represents obstacles requiring bypass. During path planning, the robot's end-effector suction cup is treated as a point. To ensure collision avoidance, obstacle boundaries undergo expansion processing: (1) Bypass-required obstacles have their boundaries expanded outward by half the robot's upper/lower platform width; (2) For traversable/step-on obstacles, boundaries are adjusted by expanding/contracting outward/inward by the suction cup radius. Solid lines depict actual obstacle boundaries, while dashed lines indicate processed boundaries after expansion/contraction adjustments.

https://doi.org/10.1017/S0263574726103580 Published online by Cambridge University Press

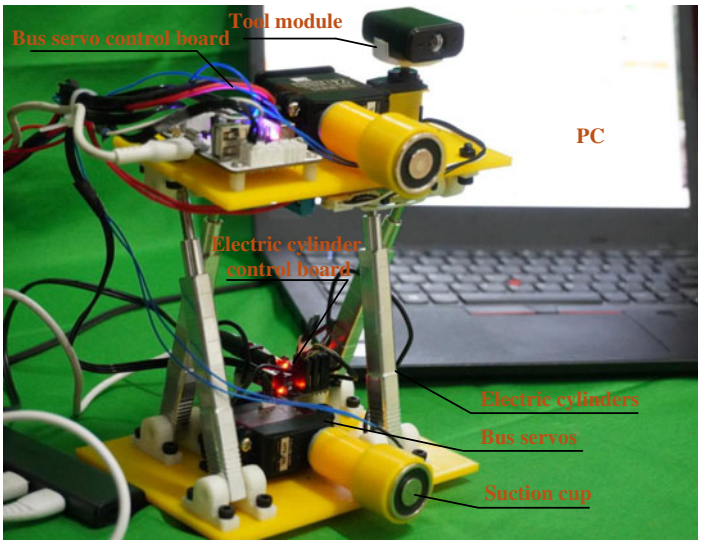


Figure 14. *Climbing robot model.*

As shown in the figure, the traditional A* algorithm can only bypass obstacles, while the improved A* algorithm fully leverages the CR's obstacle-surmounting capabilities. When encountering traversable or step-on obstacles, the algorithm calculates the cost of crossing/stepping versus bypassing, prioritizing paths with lower costs.

4.3.3 Single-step motion planning simulation

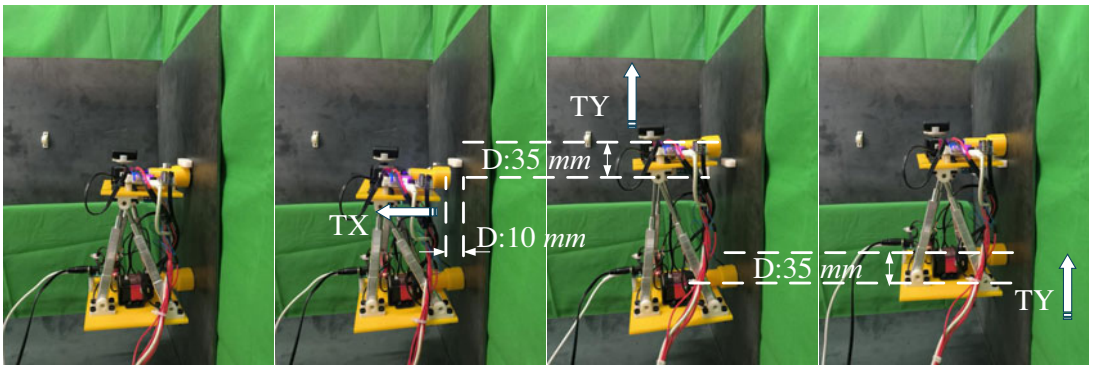
At present, the APF algorithm is relatively mature, and the singularities of the robot in the working space proposed in this paper can be avoided, and the members in the mechanism will not collide with each other when they are staggered with each other. Therefore, only the case at the end of the robot adsorption unit needs to be considered. Trajectories generated through the APF method are incorporated into the robot's kinematic equations to compute drive joint displacements, followed by simulation validation in SolidWorks. The simulation results meet the requirements of collision-free single-step motion.

5. Prototypes and experiments

The physical prototype of the mechanism is illustrated in Figure 14. The replaceable tool module is a camera, the adsorption device is an electromagnetic suction cup, the rotating device is driven by a bus servo, and the PM's actuators are electric cylinders. The driving device in the mechanism includes four electric cylinders (LA150-02D), two bus servos (HTS-20L), and two electromagnetic suction cups (AHP34). The control system of the mechanism comprises one electric cylinder control board (AEF-LA-85) and one bus servo control board (HTS-20L), with the two electromagnetic suction cups also being controlled by the servo control board. Ultimately, the motion of the CR is governed by the computer in collaboration with the control boards. The parameters of the actuation devices in the mechanism are as follows: the electric cylinders weigh 110 g, have a stroke of 50 mm, a maximum speed of 17 mm/s, and a maximum thrust of 80 N. The bus-servos weigh 65g each, provide a maximum torque of 20 kg cm, and are capable of 240° rotation. The electromagnetic suction cups weigh 30g each and provide an adhesion force of 15 kg. The overall mass of the mechanism is approximately 0.8 kg.

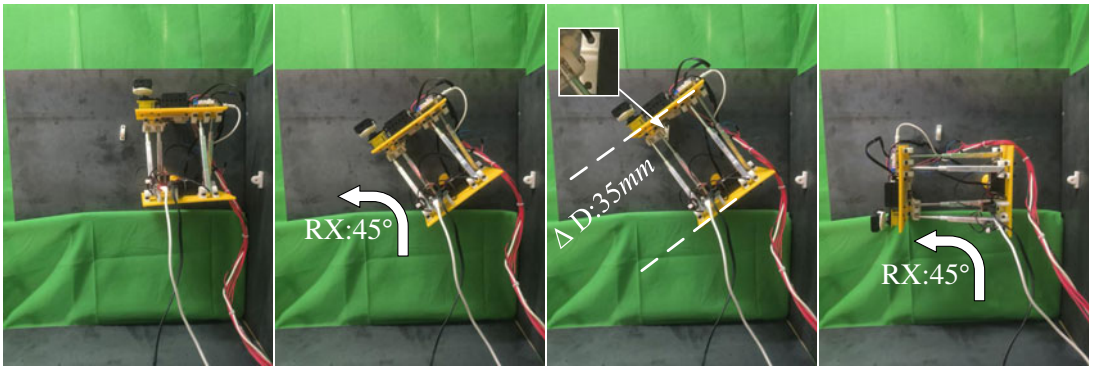
To verify the feasibility of the CR, actual climbing experiments were conducted on a single planar surface. The experiments were carried out on an iron plate (500 mm*300 mm*3 mm). To increase the complexity of the task, obstacles (The height is 7 mm) were added to the surface, as illustrated in Figure 15.

https://doi.org/10.1017/S0263574726103580 Published online by Cambridge University Press



(a) (b) (c) (d)

Figure 15. *Gait 1 climbing process.*



(a) (b) (c) (d)

Figure 16. *Gait 2 climbing process.*

The motion process of the CR during the experiment is as follows: In the initial state, both upper and lower suction cups adhered to the wall surface. First, the upper suction cup was released, and the robot's upper platform moved 10 mm away from the wall under the coordinated operation of the four actuators in the PM to avoid the obstacle. The robot then ascended 35 mm, positioning the upper suction cup above the white obstacle. Subsequently, the upper platform moved 10 mm toward the wall surface, and the upper suction cup was engaged. The lower platform then repeated the same ascending process to move upward by 35 mm.

Figure 16 illustrates the combined linear and rotational motion experiment of the CR. The specific experimental procedure is as follows: In the initial state, both suction cups adhere to the wall surface. First, the upper suction cup is released, and the lower rotating mechanism drives the robot to rotate counterclockwise by 45°. Upon encountering the white obstacle (as shown in the figure), the upper platform moves away from the wall surface by a safe distance. The PM then extends the robot by 35 mm to traverse the white obstacle. After obstacle avoidance, the lower rotating mechanism continues to drive the robot to rotate counterclockwise by an additional 45° to reach the designated position.

The results of the aforementioned two experiments demonstrate that the CR achieves motion within the wall surface, possesses obstacle-crossing capability, and meets the design requirements.

Figure 17 illustrates the overall experiment of the CR, with the specific process as follows: (a) Initially, both upper and lower suction cups adhere to the surface. (b) The lower suction cup is released and moves a preset safe distance away from the wall. (c) The robot's lower platform is driven to a designated position by the upper rotating mechanism. (d) The lower suction cup adsorption, and the upper suction cup is released. The lower rotating mechanism drives the robot to rotate until the upper and lower suction

https://doi.org/10.1017/S0263574726103580 Published online by Cambridge University Press

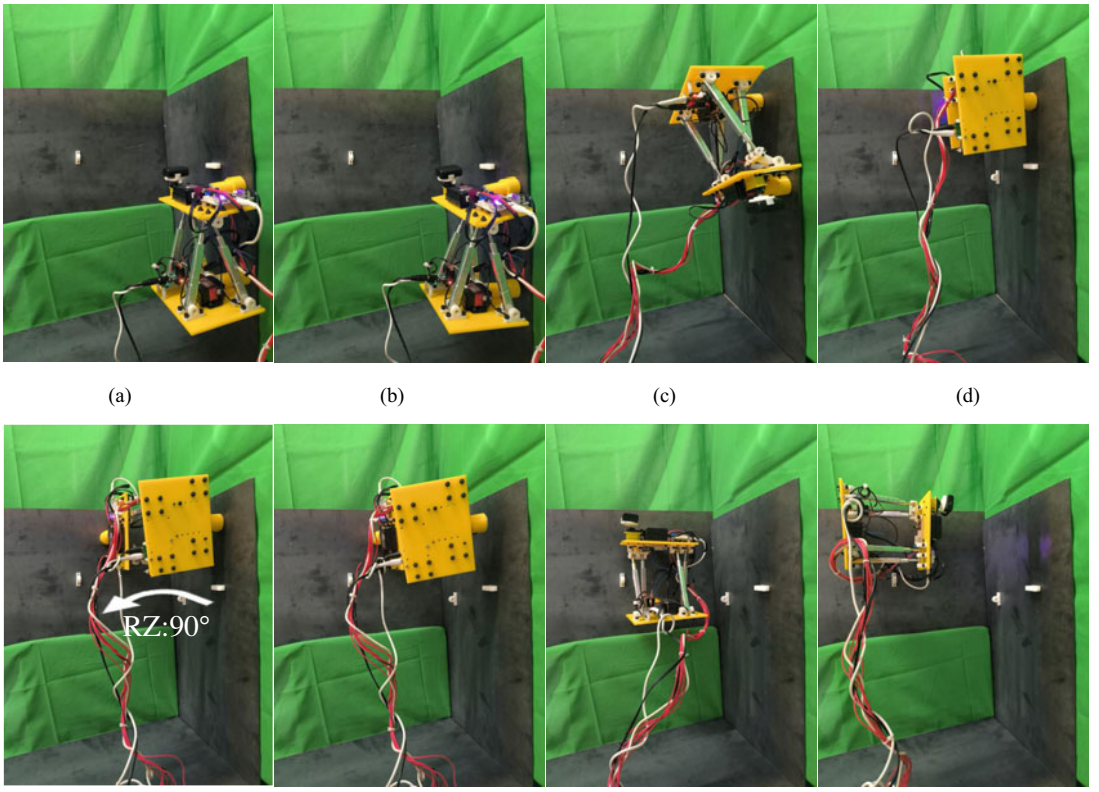


Figure 17. *3D Climbing experiments.*

cups are horizontally aligned, with the upper and lower platforms parallel. (e) After the upper platform rotates 90° under the actuation of the PM, it moves to the adjacent wall surface, and the upper suction cup adheres. (f) The lower suction cup is released and moves a certain distance away from the wall (ensuring no collision between the lower platform and the wall). (g) The upper rotating mechanism drives the CR to rotate toward the next wall surface, and the PM actuates the robot to move closer to the wall. (h) The upper rotating mechanism drives the robot to the target position.

6. Conclusion

This paper presents a CR that integrates a kinematic redundant PM as its core structure, with a serial mechanism, to substitute human workers in hazardous environments. Analysis of the DOF, position, velocity, singularities, and workspace is conducted for the PM within the CR. Based on the three-layer framework, improvements have been made to apply it to the CR. The path planning takes into account factors such as the robot's kinematics, environmental obstacles, and path length, aiming to achieve a useful and efficient path planning solution. Kinematic simulation experiments were conducted for the PM, and layered simulations of the three-layer framework were carried out. The simulation results meet the required specifications, and then a prototype was built and tested in a climbing environment. The experimental results satisfy the design requirements. Currently, the robot's components and drives are implemented in simple modules. In the future, it will be optimized accordingly so that it can be used in real production. In the path planning algorithm of this paper, the three-dimensional model is processed based on known parameters. Future work will involve adding the corresponding modules to enable real-time online path planning.

https://doi.org/10.1017/S0263574726103580 Published online by Cambridge University Press

Author contributions. Wei Ye and Tongwang Huo conceived and designed the study. Wei Ye conducted the kinematic analysis. Tongwang Huo conducted the path planning. Tongwang Huo and Xintian Feng finished the experiments. Wei Ye, Tongwang Huo, and Xintian Feng wrote the article.

Funding statement. The work is supported by the National Natural Science Foundation of China (NSFC) under Grant No. 52375033, and the Natural Science Foundation of Zhejiang Province under Grant No. ZCLZ24E0501.

Competing interests. The authors declare no conflicts of interest exist.

Ethical standards. None.

Use of AI. None.

References

[1] R. Bogue, "Climbing robots: Recent research and emerging applications," *Ind. Robot*. **46**(6), 721–727 (2019).
[2] A. Brusell, G. Andrikopoulos and G. Nikolakopoulos, "A Survey on Pneumatic Wall-climbing Robots for Inspection," **In:** *2016 24th Mediterranean Conference on Control and Automation (MED)*, IEEE (2016) pp. 220–225.
[3] Y. Dai, S. Li, X. Rui, C. Xiang and X. Nie, "Review of key technologies of climbing robots," *Front. Mech. Eng*. **18**(4), 48 (2023).
[4] S. Nansai and R. E. Mohan, "A survey of wall climbing robots: Recent advances and challenges," *Robotics* **5**(3), 14 (2016).
[5] D. Schmidt and K. Berns, "Climbing robots for maintenance and inspections of vertical structures—A survey of design aspects and technologies," *Robot. Auton. Syst*. **61**(12), 1288–1305 (2013).
[6] S. Hu, R. Peng, K. He, J. Li, J. Cai and W. Zhou, "Structural Design and Magnetic Force Analysis of a New Crawler-type Permanent Magnetic Adsorption Wall—Climbing," **In:** *2017 IEEE International Conference on Information and Automation (ICIA)*, IEEE (2017) pp. 598–603.
[7] J. Cai, K. He, H. Fang, H. Chen, S. Hu and W. Zhou, "The Design of Permanent-magnetic Wheeled Wall-climbing Robot," **In:** *IEEE International Conference on Information and Automation (ICIA)*, IEEE (2017) pp. 604–608.
[8] Y. Guan, H. Zhu, W. Wu, X. Zhou, L. Jiang, C. Cai, L. Zhang and H. Zhang, "A modular biped wall-climbing robot with high mobility and manipulating function," *IEEE/ASME Trans. Mechatron*. **18**(6), 1787–1798 (2012).
[9] Y. Guan, L. Jiang, H. Zhu, W. Wu, X. Zhou, C. Cai, Z. Xiao, X. Chen and H. Zhang, "Climbot: A Modular Bio-inspired Biped Climbing Robot, 2011 IEEE," **In:** *RSJ Intl Conf on Intelligent Robots and Systems*, San Francisco, CA (2011) pp. 1473–1478.
[10] Y. Guan, L. Jiang, H. Zhu, W. Wu, X. Zhou, H. Zhang and X. Zhang, "Climbot: A bio-inspired modular biped climbing robot—system development, climbing gaits, and experiments," *J. Mech. Robot*. **8**(2), 021026 (2016).
[11] R. Saltarén, R. Aracil, J. M. Sabater, O. Reinoso and L. M. Jiménez, "Modelling, Simulation and Conception of Parallel Climbing Robots for Construction and Service," **In:** *Workshop & Conf. on CLIMBING & WALKING ROBOTS (CLAWAR)*, (1999) pp. 1–13.
[12] R. Saltaren, R. Aracil, O. Reinoso and M. A. Scarano, "Climbing parallel robot: A computational and experimental study of its performance around structural nodes," *IEEE Trans. Robot*. **21**(6), 1056–1066 (2005).
[13] Y. Yao, W. Wang, Y. Qiao, Z. He, F. Liu, X. Li, X. Liu, D. Zou and T. Zhang, "A novel series-parallel hybrid robot for climbing transmission tower," *Ind. Robot*. **48**(4), 577–588 (2021).
[14] S. T. Nguyen and H. M. La, "Roller chain-like robot for steel bridge inspection," (2019).
[15] L. T. Schreiber and C. Gosselin, "Schönflies motion PARAllel robot (SPARA): A kinematically redundant parallel robot with unlimited rotation capabilities," *IEEE/ASME Trans. Mechatron*. **24**(5), 2273–2281 (2019).
[16] C. Gosselin, T. Laliberté and A. Veillette, "Singularity-free kinematically redundant planar parallel mechanisms with unlimited rotational capability," *IEEE Trans. Robot*. **31**(2), 457–467 (2015).
[17] L. T. Schreiber and C. Gosselin, "Exploiting the kinematic redundancy of a (6+3) degrees-of-freedom parallel mechanism," *J. Mech. Robot*. **11**(2), 021005 (2019).
[18] S. Luo, M. Zhang, Y. Zhuang, C. Ma and Q. Li, "A survey of path planning of industrial robots based on rapidly exploring random trees," *Front. Neurorobot* **17**, 1268447 (2023).
[19] N. K. Dhiman, D. Deodhare and D. Khemani, "A Review of Path Planning and Mapping Technologies for Autonomous Mobile Robot Systems," **In:** *Proceedings of the 5th ACM COMPUTE Conference: Intelligent & Scalable System Technologies*, (2012) pp. 1–8.
[20] Z. Han, H. Sun, J. Huang, J. Xu, Y. Tang and X. Liu, "Path planning algorithms for smart parking: Review and prospects," *World Electr. Veh. J*. **15**(7), 322 (2024).
[21] H. Zhang, W. Lin and A. Chen, "Path planning for the mobile robot: A review," *Symmetry* **10**(10), 450 (2018).
[22] Q. Yu and J. Zhou, "A Review of Global and Local Path Planning Algorithms for Mobile Robots," **In:** *2024 8th International Conference on Robotics, Control and Automation (ICRCA)*, (2024) pp. 84–90.
[23] D. Luo, X. Huang, Y. Huang, M. Miao and X. Gao, "Optimal trajectory planning for wheeled robots (OTPWR): A globally and dynamically optimal trajectory planning method for wheeled mobile robots," *Machines* **12**(10), 668 (2024).

https://doi.org/10.1017/S0263574726103580 Published online by Cambridge University Press

[24] B. Zhang, G. Li, Q. Zheng, X. Bai, Y. Ding and A. Khan, "Path planning for wheeled mobile robot in partially known uneven terrain," *Sensors* **22**(14), 5217 (2022).
[25] H. Zhu, S. Gu, L. He, Y. Guan and H. Zhang, "Transition analysis and its application to global path determination for a biped climbing robot," *Appl. Sci*. **8**(1), 122 (2018).
[26] H. Zhu, J. Lu, S. Gu, S. Wei and Y. Guan, "Planning three-dimensional collision-free optimized climbing path for biped wall-climbing robots," *IEEE/ASME Trans. Mechatron*. **26**(5), 2712–2723 (2020).
[27] M. Fabregat-Jaén, A. Peidró, P. Mollá-Santamaría, F. J. Soler and O. Reinoso, "Planificación jerárquica de movimientos de un robot trepador bípedo en estructuras tridimensionales reticulares," *Rev. Iberoam. Autom. Inform. Ind*. **21**(3), 262–273 (2024).
[28] H. Zhang, M. Liu, R. Liu and T. Hu "Path planning of robot in three-dimensional grid environment based on genetic algorithms[C]//2008 7th world congress on intelligent control and automation," *IEEE*, 1010–1014 (2008).
[29] N. He, Y. Su, X. Fan, Y. Xu and H. Wang, "Dynamic Path Planning of Mobile Robot Based on Artificial Potential Field," **In:** *2020 International Conference on Intelligent Computing and Human-Computer Interaction (ICHCI)*, IEEE (2020) pp. 259–264.
[30] C. Fan, H. Liu and Y. Zhang, "Type synthesis of 2T2R, 1T2R and 2R parallel mechanisms," *Mech. Mach. Theory* **61**, 184–190 (2013).
[31] Z. Pu and L. Jin, "Workspace analysis of a 2PRS/2PUS. 4-DOF parallel mechanism," *J. Mech. Transm*. **42**(7), 87–91 (2018).
[32] H.-R. Fang, P.-F. Liu, H. Yang and B.-S. Jiang, "Design and analysis of a novel 2T2R parallel mechanism with the closed-loop limbs," *Int. J. Autom. Comput*. **18**(4), 654–666 (2021).
[33] X. Kong and C. M. Gosselin, "Forward displacement analysis of third-class analytic 3-RPR planar parallel manipulators," *Mech. Mach. Theory* **36**(9), 1009–1018 (2001).
[34] Y. Li, L. Wang, J. Liu and Z. Huang, "Applicability and generality of the modified Grübler-Kutzbach criterion," *Chin. J. Mech. Eng*. **26**(2), 257–263 (2013).
[35] C. Gosselin and J. Angeles, "Singularity analysis of closed-loop kinematic chains," *IEEE Trans. Robotic. Autom*. **6**(3), 281–290 (1990).
[36] A. Yiğit, D. Breton and C. Gosselin, "Exploiting the kinematic redundancy of a (6+3)-degree-of-freedom parallel manipulator to produce unlimited rotation of the platform," *J. Mech. Transm*. **16**(7), 071004 (2024).
[37] I. Ebrahimi, J. A. Carretero and R. Boudreau, "3-PRRR redundant planar parallel manipulator: Inverse displacement, workspace and singularity analyses," *Mech. Mach. Theory* **42**(8), 1007–1016 (2007).
[38] M. Z. Huang and J. L. Thebert, "A study of workspace and singularity characteristics for design of 3-DOF planar parallel robots," *Int. J. Adv. Manuf. Technol*. **51**, 789–797 (2010).
[39] P. E. Hart, N. J. Nilsson and B. Raphael, "A formal basis for the heuristic determination of minimum cost paths," *IEEE T. Syst. Sci. Cyb*. **4**(2), 100–107 (1968).

Cite this article: W. Ye, T. Huo and X. Feng (2026). "Mechanism design and trajectory planning of a kinematically redundant parallel climbing robot", Robotica **44**, 1305–1324. https://doi.org/10.1017/S0263574726103580

https://doi.org/10.1017/S0263574726103580 Published online by Cambridge University Press